Structure of human Ca$_v$2.2 channel blocked by the pain killer ziconotide

Shuai Gao[1,2], **Xia Yao**[1,2], **Nieng Yan**[1,3]

[1]Department of Molecular Biology, Princeton University, Princeton, NJ 08544, USA

Abstract

The neuronal-type (N-type) voltage-gated calcium (Ca$_v$) channels, which are designated Ca$_v$2.2, have an important role in the release of neurotransmitters[1–3]. Ziconotide is a Ca$_v$2.2-specific peptide pore blocker that has been clinically used for treating intractable pain[4–6]. Here we present cryo-electron microscopy structures of human Ca$_v$2.2 (comprising the core α1 and the ancillary α2δ−1 and β3 subunits) in the presence or absence of ziconotide. Ziconotide is thoroughly coordinated by helices P1 and P2, which support the selectivity filter, and the extracellular loops (ECLs) in repeats II, III and IV of α1. To accommodate ziconotide, the ECL of repeat III and α2δ−1 have to tilt upward concertedly. Three of the voltage-sensing domains (VSDs) are in a depolarized state, whereas the VSD of repeat II exhibits a down conformation that is stabilized by Ca$_v$2-unique intracellular segments and a phosphatidylinositol 4,5-bisphosphate molecule. Our studies reveal the molecular basis for Ca$_v$2.2-specific pore blocking by ziconotide and establish the framework for investigating electromechanical coupling in Ca$_v$ channels.

Ca$_v$2.2 channels are also known as the N-type Ca$_v$ channels for their role in transmitter release in the central and peripheral nervous systems. Combining different splice forms of the voltage-dependent Ca^{2+} conducting core subunit α1 with auxiliary subunits—including the extracellular α2δ and the cytosolic β subunits—yields various Ca$_v$2.2 heteromers that exhibit distinct membrane distribution and biophysical properties[1,2,7,8]. Ca$_v$2.2 channels in the primary afferent terminals are involved in pain signalling. Suppression of Ca$_v$2.2 activity thus represents a strategy for the development of analgesic agents[9–11].

Ca$_v$2.2 can be potently and selectively inhibited by a number of peptide toxins, some of which have been exploited for pharmacological applications[3,12–14]. Among these, the

ω-conotoxin MVIIA was developed to produce ziconotide (also known as SNX-111 and Prialt), which has been approved by the US Food and Drug Administration for the treatment of severe pain[4–6]. However, its intrathecal application and adverse effects have limited the broad use of ziconotide[15,16]. High-resolution structures of ziconotide-bound $Ca_v2.2$ are required to elucidate the molecular basis for the subtype-specific inhibition and to facilitate drug discovery.

Cryo-electron microscopy (cryo-EM) structures of rabbit $Ca_v1.1$ and human $Ca_v3.1$ alone and in complex with various modulators have previously been published[17–21]. Despite substantial sequence variations, the structures of $Ca_v1.1$ and $Ca_v3.1$ are similar in their transmembrane regions, which comprise four homologous repeats (designated I, II, III and IV; throughout, subscript Roman numerals indicate location on the respective homologous repeat) each. The transmembrane segments 5 and 6 (S5 and S6) from the four repeats enclose the central pore domain that is surrounded by the four VSDs, each of which is constituted by S1 to S4 (Supplementary Fig. 1). In contrast to the conserved transmembrane domain, the long linkers between the repeats (the I–II linker and the II–III linker) and the C-terminal segments vary substantially both in length and in the primary sequence. These cytosolic segments remain unresolved in the structures of Ca_v and closely related Na_v channels.

The gating of the pore domain is coupled to the movements of VSDs in response to membrane potential changes, in a mechanism that is known as the electromechanical coupling. Despite minor deviations, all of the previously reported structures of $Ca_v1.1$ and $Ca_v3.1$ channels exhibit similar 'inactivated' states, in which the pore domain is closed and all four VSDs are in the 'up' conformations[18–21]. Investigating electromechanical coupling necessitates structural resolution of the channels in distinct conformations.

Cryo-EM analysis of the $Ca_v2.2$ complex

Details of protein production and cryo-EM analysis of human $Ca_v2.2$ in the absence (apo) and presence of purchased ziconotide (determined at 3.1 and 3.0 Å resolution, respectively (Extended Data Fig. 1)) are provided in the Methods. The 3D electron microscopy reconstructions of apo $Ca_v2.2$ and $Ca_v2.2$–ziconotide are nearly identical, and show only limited structural deviations. Unless indicated otherwise, the structural analysis discussed below is based on $Ca_v2.2$–ziconotide because of its higher resolution.

We could reliably assign side chains to α1, α2δ−1, ziconotide and the α1-interacting guanylate kinase domain of β3 (Extended Data Figs. 2–4, Extended Data Table 1, Supplementary Video 1). The distal domain of β3 and the C-terminal domain of α1 were docked as rigid bodies. In addition to the protein components, one Ca^{2+} ion is coordinated by the signature EEEE motif[22] (Glu314, Glu663, Glu1365 and Glu1655) at the outer site of the selectivity filter (Extended Data Fig. 3c). Sixteen sugar moieties were assigned to eight glycosylated Asn residues (seven on α2δ−1 and one on α1). Among the resolved cholesterol, phospholipid and detergent molecules that surround α1, a phosphatidylinositol 4,5-bisphosphate (PIP_2) molecule binds to the interface of VSD_{II} and the pore domain in the inner leaflet (Fig. 1a, Extended Data Fig. 4).

The overall structures of apo Ca$_v$2.2 and rat Ca$_v$1.1 can be superimposed with a root mean square deviation of 1.10 Å over 1,728 Cα atoms. The α2δ−1 subunit and its interface with the extracellular segments of α1 remain identical, despite minor structural differences in ECL$_I$ and ECL$_{III}$ (Extended Data Fig. 5). On the cytosolic side, the helix after S6$_I$ bends to be parallel with the membrane plane and interacts with β3 through its α1-interacting domain (AID) motif[23]. We refer to this transverse helix as the AID helix. These common structures—which have been illustrated in detail for Ca$_v$1.1[18]—are not discussed further here: here we focus on ziconotide recognition and repeat II, which exhibits several features that are distinct from known structures of eukaryotic Ca$_v$ and Na$_v$ channels, for detailed analysis.

Pore blockade of Ca$_v$2.2 by ziconotide

Ziconotide has previously been reported to specifically block Ca$_v$2.2 with a half-maximal inhibitory concentration of 0.7–1.8 nM[24,25]. Our structure reveals that the blocker, which contains three disulfide bonds, is nestled in the electronegative cavity that surrounds the entrance to the selectivity filter, and that specific recognition is mediated mainly by charged and polar residues on the P1 and P2 helices and the ECLs in repeats II, III and IV. Although ECL$_I$ is also in the vicinity of ziconotide, none of the repeat I residues is directly engaged in ziconotide coordination (Fig. 1b, c, Extended Data Fig. 6a).

The binding pose of ziconotide is reminiscent of that of μ-conotoxin KIIIA (KIIIA) in its complex structure with Na$_v$1.2, in which Lys7 of KIIIA points to the outer mouth of the selectivity filter[26] (Extended Data Fig. 6b). Ziconotide does not possess an equivalent residue to directly seal the entrance to the vestibule of the selectivity filter. Instead, it blocks ion entrance by neutralizing the outer electronegativity and sterically hindering the ion access path to the entrance of the selectivity filter (Fig. 1b). To neutralize the acidic residues, ziconotide engages Arg10 and Tyr13 to bind to Asp664, which marks the beginning of P2$_{II}$. Ser19 interacts with Glu1659, which is on the first helical turn of P2$_{IV}$. Thr17 interacts with Asp1345 on ECLIII, and Arg21 and Lys4 interact with Asp1628 and Asp1629, respectively, on ECLIV (Fig. 1c).

Our structure-guided sequence comparison showed that four of the eight ziconotide-coordinating residues in Ca$_v$2.2 (Thr643, Asp1345, Lys1372 and Asp1629) are not conserved in other Ca$_v$ channels (Fig. 1c, Supplementary Fig. 1), which explains the subtype specificity of pore blockade by ziconotide. Consistent with our structure, Y13A or R10A substitutions have previously been shown to substantially reduce pore blocking by ziconotide, and Y13R abolished its activity [24,27,28].

The only structural change upon ziconotide binding is a slight tilt of α2δ−1 and ECL$_{III}$ of α1 as a rigid body. The upward movement of ECL$_{III}$ is necessary to avoid a clash with ziconotide (Fig. 1d, Extended Data Fig. 6c, d). The α2δ−1 subunit has previously been shown to reduce ziconotide affinity[29], which may result from the energy penalty for lifting ECL$_{III}$ and α2δ−1 to accommodate ziconotide.

Cytosolic segments unique to Ca_v2

On the cytosolic side, $S6_{II}$ is extraordinarily long and contains seven additional helical turns (residues 714 to 739), which we designate the cytosolic segment of $S6_{II}$ ($S6_{II}C$). The ensuing sequence (residues 740 to 786) forms two additional helices (which we designate cytosolic helix $(CH)1_{II}$ and $CH2_{II}$) that fold back towards the membrane. $CH1_{II}$ is anti-parallel with $S6_{II}C$, whereas $CH2_{II}$ is perpendicular to it (Fig. 2a). $S6_{II}C$ is not conserved among the three Ca_v families and the sequence corresponding to $CH1_{II}$ and $CH2_{II}$ is missing in Ca_v1 and Ca_v3 families, which affords an explanation for the lack of these structural elements in $Ca_v1.1$ and $Ca_v3.1$[18,20] (Supplementary Fig. 1).

The U-turn between $S6_{II}C$ and $CH1_{II}$ mediates weak interaction with β3, in addition to the well-characterized primary interface between the AID and the guanylate kinase domain of β3[30–32] (Fig. 2b). Glu740, which is conserved in Ca_v2 family only and marks the end of $S6_{II}$, may be hydrogen-bonded to His348 on the α9 helix of β3. Glu743, which is positioned at the tip of the U-turn, may interact with the amide of Glu111 in the SH3 domain of β3 (Fig. 2b inset). With this additional interface, β3 is sandwiched between AID and $S6_{II}$.

$CH1_{II}$ has only limited contact with $S6_{II}C$, whereas $CH2_{II}$ interacts with all four S6 segments (Fig. 2c). As the sequence corresponding to $CH2_{II}$ is not found in Ca_v1 and Ca_v3 channels, this structural feature is probably unique to Ca_v2 channels (Supplementary Fig. 1). To accommodate $CH2_{II}$, the last three helical turns in $S6_{III}$ are unwound, resulting in a shorter $S6_{III}$ than that in $Ca_v1.1$. The N-terminal residues of $CH2_{II}$ are placed immediately beneath the closed intracellular gate (Fig. 2d, e)

The intracellular gate of $Ca_v2.2$ comprises a large number of residues that intertwine to form a hydrophobic structural core. At the bottom of this exceptionally thick hydrophobic gate is Trp768 on $CH2_{II}$, which is surrounded by Ala360, Ala713, Ile1417 and Phe1711 from the four S6 segments (Fig. 2e insets). By pulling all four S6 segments together and directly engaging Trp768 to secure the gate, $CH2_{II}$ may facilitate the closing of the pore domain.

VSD_{II} in a 'down' conformation

The four VSDs of $Ca_v2.2$ carry different numbers of gating charge residues: five in VSD_I (R1 to R4, and K5; to make the numbering of the gating charge residues consistent, we designate the residue on the first helical turn of the S4 segment as 1), VSD_{II} (R2, R3, R4, K5 and K6) and VSD_{IV} (R2, R3, R4, K5 and R6), and six in VSD_{III} (K1, R2, R3, R4, K5 and K6) (Fig. 3a). K5 in VSD_I, K5 and K6 in VSD_{III} and K5 and R6 in VSD_{IV} are below, and the other gating charge residues are above, the occluding Phe on S2 (a state that we define as up). By contrast, in VSD_{II} R3, R4, K5 and K6 are all below the occluding Phe525, and only R2 is above it (a state that we define as down) (Fig. 3a). When the four VSDs are superimposed, $S4_{II}$ slides down by about 11–12 Å from the other S4 segments, and the S1, S2 and S3 segments are relatively well superimposed (Fig. 3b).

In VSD_I, VSD_{III} and VSD_{IV}, the one or two extracellular helical turns of S4 are in the form of an α-helix, and the remaining segments conform to a 3_{10} helix. In VSD_{II}, the entire S4 is a 3_{10} helix, and R2, R3, R4 and K5 all line the same side. K6 (Lys590), which is at the tip

of a sharp and short turn that immediately precedes the S4–5$_{II}$ segment, is on the opposite side to the other four gating charge residues and its side chain projects into the cytosol (Fig. 3a, b). Compared to the deactivated structures of toxin-bound VSD$_{IV}$ in the Na$_v$PaS-1.7 chimera[33] and rat Na$_v$1.5[34], S4$_{II}$ in Ca$_v$2.2 is lower by one more helical turn (Extended Data Fig. 7a).

Structural comparison of the α1 subunits in Ca$_v$2.2 and Ca$_v$1.1 shows that the pore domain, VSD$_I$ and VSD$_{IV}$ remain nearly identical. Major shifts occur in repeats II and III (Fig. 3c, Extended Data Fig. 7b). VSD$_{III}$ undergoes a slight clockwise rigid-body rotation from Ca$_v$1.1 to Ca$_v$2.2 in the intracellular view. The motion of VSD$_{II}$ involves both domain rotation and intradomain rearrangement (Fig. 3c, d, Extended Data Fig. 7c, d, Supplementary Video 2). The S1, S2 and S3 segments in VSD$_{II}$ of Ca$_v$1.1 and Ca$_v$2.2 remain nearly identical in domain comparison, whereas S4 is dislodged by about 12 Å towards the intracellular side from Ca$_v$1.1 to Ca$_v$2.2 through a spiral sliding, leading to the transfer of two gating charge residues (R3 and R4) across the occluding Phe on S2 (Extended Data Fig. 7d). The most marked shift occurs to K6, the amine group of which is displaced by 25 Å through both secondary structure transition and side-chain swing (Fig. 3d, Supplementary Video 2).

Accompanying the rotation of VSD$_{II}$ and the marked shift of S4$_{II}$ from Ca$_v$1.1 to Ca$_v$2.2, the ensuing N terminus of S4–5$_{II}$ is pushed down by about 3 Å. The motion of S4–5$_{II}$ drives the adjacent S6$_{II}$C to shift accordingly, establishing a potential transmission path from VSD$_{II}$ motion to pore gating (Fig. 3d, Extended Data Fig. 8, Supplementary Video 2). As only VSD$_{II}$ is in the down conformation and the other VSDs are up, we refrain from assigning a functional state to the present Ca$_v$2.2 structure. As, to our knowledge, a down structure of a VSD has not previously been captured in the absence of mutagenesis or modulators, we attempt to identify the structural elements that stabilize the deactivated state of VSD$_{II}$.

Stabilization of the down VSD$_{II}$ by PIP$_2$

The intracellular segments that are unique to Ca$_v$2 contribute to the stabilization of the down conformation of VSD$_{II}$. S6$_{II}$C, which interacts extensively with S4–5$_{II}$, contacts the AID helix and CH2$_{II}$ through several polar residues (Fig. 4a). The AID helix binds S0, S2 and S3 in VSD$_{II}$, preventing rotation of these segments. Simultaneous association of S0$_{II}$, S2–3$_{II}$, S4–5$_{II}$ and S6$_{II}$C with the straight AID helix may restrain VSD$_{II}$ from rotation, therefore stabilizing the present conformation. More than half of the residues in the extensive interaction network are Ca$_v$2-specific, which provides a potential explanation for the distinct VSD$_{II}$ conformations in Ca$_v$2.2 (Fig. 4a, b).

The bound PIP$_2$ also appears to favour a down VSD$_{II}$, as its binding pose is incompatible with the up conformation of Ca$_v$1.1 VSD$_{II}$. The head group of PIP$_2$ wedges into a cytosolic cavity in VSD$_{II}$ through the interface of S3 and S4, and the tails are coordinated by hydrophobic residues on S3 toS6 in repeat II and S5 and S6 in repeat III (Fig. 4c, Extended Data Fig. 9a, b). The PIP$_2$-binding site is reminiscent of that in KCNQ1[35], but is at a higher position (Extended Data Fig. 9c). The 5-phosphate group of PIP$_2$ is coordinated by R4 (Arg584) and K5 (Lys587) on S4$_{II}$. The head group is anchored by Ser544 (which marks

the beginning of $S3_{II}$), the amide group of Phe546 and Arg596 on $S4-5_{II}$ (Fig. 4c, Extended Data Fig. 9a). When VSD_{II} moves upward, its interface with the neighbouring $S5_{III}$ is also rearranged (Extended Data Fig. 9d). Consequently, PIP_2, the displacement of which may be restrained by the hydrophobic membrane, can no longer retain these polar and hydrophobic interactions, but clashes with the lifted $S4-5_{II}$ (Fig. 4c, Extended Data Fig. 9a). Therefore, the bound PIP_2 may stabilize the down conformation of VSD_{II}.

Discussion

The cryo-EM structures of the human $Ca_v2.2$ complex reveal the molecular basis for the specific pore blockade of $Ca_v2.2$ by ziconotide and provide a mechanistic interpretation for lowered ziconotide affinity in the presence of $α2δ-1$ (Fig. 1d). The down conformation of VSD_{II}, which is stabilized by previously unresolved cytosolic segments and a PIP_2 molecule, provides important insights into the electromechanical coupling in Ca_v channels.

The AID helix, which follows $S6_I$ through a tight turn and interacts with $S6_{II}$, is sandwiched by VSD_{II} and β3 (Fig. 4b). It may thus serve as a lever to couple the conformational changes of VSD_{II} with $S6_I$, $S6_{II}$ and the intracellular segments. The β subunits may also modulate channel activity in part through the interaction with AID.

PIP_2 has previously been shown to both cause a right shift of the activation voltage and reduce the current rundown of $Ca_v2.1$[36]. The PIP_2-binding site observed in this study may account for the voltage-dependent inhibitory modulation as it stabilizes the down conformation of VSD_{II}. It remains to be investigated whether a separate PIP_2-binding site is responsible for the voltage-independent rundown reduction, a mechanism that may involve $G_{βγ}$ proteins[37]. Structural elucidation of representative members in the three Ca_v families lay the foundation for future structural and mechanistic investigation of the electromechanical coupling and the regulation of Ca_v channels by a variety of modulators[3,8].

METHODS

No statistical methods were used to predetermine sample size. The experiments were not randomized, and investigators were not blinded to allocation during experiments and outcome assessment.

Transient expression of the human $Ca_v2.2$ complex in HEK293F cells

Codon-optimized cDNAs of *CACNA1B* for full-length $Ca_v2.2$ α1 (2,339 residues, Uniprot Q00975–1), *CACNA2D1* for $α2δ-1$ (1,103 residues, Uniprot P54289–1) and *CACNB3* for β3 (484 residues, Uniprot P54284–1) were synthesized (BGI Geneland Scientific) and subcloned into the pCAG vector. An amino-terminal Flag tag and a carboxy-terminal His_{10} tag were added to each subunit in $Ca_v2.2$–ziconotide and untagged $α2δ-1$ was used for the apo $Ca_v2.2$ complex. DNA sequences were examined in SnapGene. HEK293F suspension cells (Thermo Fisher Scientific, R79007) were cultured in Freestyle 293 medium (Thermo Fisher Scientific) at 37 °C, supplied with 5% CO_2 under 60% humidity. When cell density reached $1.5-2.0 \times 10^6$ cells per ml, a mixture of expression plasmids and polyethylenimine (Polysciences) was added into cell culture to initiate the transient expression of human

$Ca_V2.2$ following a standard transfection protocol. No further authentication was performed for the commercially available cell line. *Mycoplasma* contamination was not tested.

Protein purification of human $Ca_V2.2$ and complex preparation with ziconotide

Approximately 72 h after transfection, the HEK293F cells were collected by centrifugation at $3,600g$ for 10 min and resuspended in the lysis buffer containing 25 mM HEPES (pH 7.4), 150 mM NaCl and the protease inhibitor cocktail containing 2.6 μg ml^{-1} aprotinin and 1.4 μg ml^{-1} pepstatin. The suspension was supplemented with glyco-diosgenin (GDN) (Anatrace) to a final concentration of 1% (w/v), *n*-dodecyl-β-D-maltopyranoside (DDM, Anatrace) to 0.2% (w/v), and cholesteryl hemisuccinate Tris salt (CHS) (Anatrace) to 0.04% (w/v). After incubation at 4 °C overnight, the mixture was centrifuged at $35,000g$ for 30 min, and the supernatant was applied to anti-Flag M2 affinity resin (Sigma). The resin was rinsed with wash buffer (buffer W) containing 25 mM HEPES (pH 7.4), 150 mM NaCl, 2 mM $CaCl_2$ and 0.01% GDN. Eluted with buffer W plus 0.2 mg ml^{-1} Flag peptide (synthesized by GenScript), the eluent was concentrated using a 100-kDa cut-off Amicon (Millipore) and further purified through size-exclusion chromatography (Superose 6 10/300 GL, GE Healthcare) that was preequilibrated in buffer W. The peak fractions were pooled and concentrated to a concentration of about 20 mg ml^{-1} with $\alpha2\delta-1$ in excess. For structural determination of $Ca_V2.2$–ziconotide, purchased ziconotide (Alomone labs) was added to the concentrated protein solution at a final concentration of 2 mg ml^{-1}. The mixture was incubated at 4 °C for 30 min before making cryo-grids.

Cryo-EM sample preparation and data collection

Aliquots of 3.5 μl concentrated apo $Ca_V2.2$ or $Ca_V2.2$–ziconotide were loaded onto glow-discharged holey carbon grids (Quantifoil Cu R1.2/1.3, 300 mesh for $Ca_V2.2$–ziconotide, Quantifoil Au R1.2/1.3, 300 mesh for the apo channel), which were blotted for 6 s and plunge-frozen in liquid ethane cooled by liquid nitrogen using a Vitrobot Mark IV (Thermo Fisher) at 8 °C with 100% humidity. Grids were transferred to a Titan Krios electron microscope (Thermo Fisher) operating at 300 kV and equipped with a Gatan Gif Quantum energy filter (slit width 20 eV) and spherical aberration (Cs) image corrector. Micrographs were recorded using a K2 Summit counting camera (Gatan) in super-resolution mode with a nominal magnification of 105,000×, resulting in a calibrated pixel size of 0.557 Å. Each stack of 32 frames was exposed for 5.6 s, with an exposure time of 0.175 s per frame. The total dose for each stack was about 50 e$^-$ per Å^2. SerialEM was used for fully automated data collection[38]. All 32 frames in each stack were aligned, summed and dose-weighted using MotionCorr2[39] and twofold-binned to a pixel size of 1.114 Å per pixel. The defocus values were set from −1.9 to −2.1 μm and estimated by Gctf[40].

Image processing

A total of 3,384 and 1,317 cryo-EM micrographs were collected for $Ca_V2.2$–ziconotide and the apo channel, respectively, and 1,909,156 ($Ca_V2.2$–ziconotide) and 928,665 (apo $Ca_V2.2$) particles were auto-picked by RELION-3.0. Particle picking was performed using 2D classes of rabbit $Ca_V1.1$ (EMD-22426) in the side and tilted views as reference. All subsequent 2D and 3D classification and refinement was performed with RELION-3.0[41]. Two rounds of reference-free 2D classification were performed to remove ice spots,

contaminants and aggregates, yielding 1,101,746 and 807,595 particles for $Ca_v2.2$–ziconotide and apo $Ca_v2.2$, respectively. The particles were processed with a global search with $K = 1$ to determine the initial orientation alignment parameters using bin2 particles. The electron microscopy map of rabbit $Ca_v1.1$ (EMD-22426), low-pass-filtered to 20 Å, was used as an initial reference[21]. The output of the 35–40 iterations was further applied to local angular search 3D classification with four classes. A total of 305,200 and 159,079 particles (for $Ca_v2.2$–ziconotide and apo $Ca_v2.2$, respectively) were selected by combining the good classes of the local angular search 3D classification. The particles were then re-extracted using a box size of 280 and pixel size of 1.114 Å. These particles yielded reconstructions at 3.2 Å and 3.3 Å (for $Ca_v2.2$–ziconotide and apo $Ca_v2.2$, respectively) after 3D auto-refinement with an adapted mask. Multi-reference 3D classification using bin1 particles after Bayesian polishing resulted in a reconstruction at 3.0 Å from 170,839 particles for $Ca_v2.2$–ziconotide and 3.1 Å from 56,616 particles for the apo channel. Focused refinement was performed using a core mask for β3 and α1 $S6_{II}$.

All 2D classification, 3D classification and 3D auto-refinement was performed with RELION 3.0. Resolutions were estimated using the gold-standard Fourier shell correlation 0.143 criterion with high-resolution noise substitution[42,43].

Model building and refinement

$Ca_v2.2$, together with the other two Ca_v2 subtypes ($Ca_v2.1$ and $Ca_v2.3$) and the four Ca_v1 subtypes ($Ca_v1.1$ to $Ca_v1.4$), are high-voltage-activated, in contrast to the low-voltage-gated $Ca_v3.1$, $Ca_v3.2$ and $Ca_v3.3$ channels[44] (Supplementary Fig. 1). Model building of $Ca_v2.2$ was thus based on the structure of the $Ca_v1.1$ channel complex. The starting model of $Ca_v2.2$ α1 subunit and α2δ−1 were built in SWISS-MODEL[45] based on the structure of rabbit $Ca_v1.1$ (PDB code 5GJW), and that of β3 was based on the crystal structure of rat β3 (PDB code 1VYU). The starting models of $Ca_v2.2$ and ω-conotoxin MVIIA (PDB code 1OMG) were then manually docked into the 3.0 Å toxin-bound electron microscopy map in Chimera[46]. The model was manually adjusted in COOT[47], followed by refinement against the corresponding maps by phenix.real_space_refine program in PHENIX[48] with secondary structure and geometry restraints. For model building of the apo channel, coordinates for $Ca_v2.2$ α1, α2δ−1 and β3 were docked into the 3.1 Å apo $Ca_v2.2$ map separately and manually adjusted in COOT.

The excellent map quality supports reliable assignment of 2,622 side chains in both structures. Similar to the structures of other eukaryotic Ca_v and Na_v channels[18,20,49–56], most of the cytosolic segments in the α1 subunit are invisible, including residues 1–85 in the N terminus, residues 407–463 in the I–II linker, residues 787–1138 in the II–III linker, and residues 1838–2339 in the C terminus.
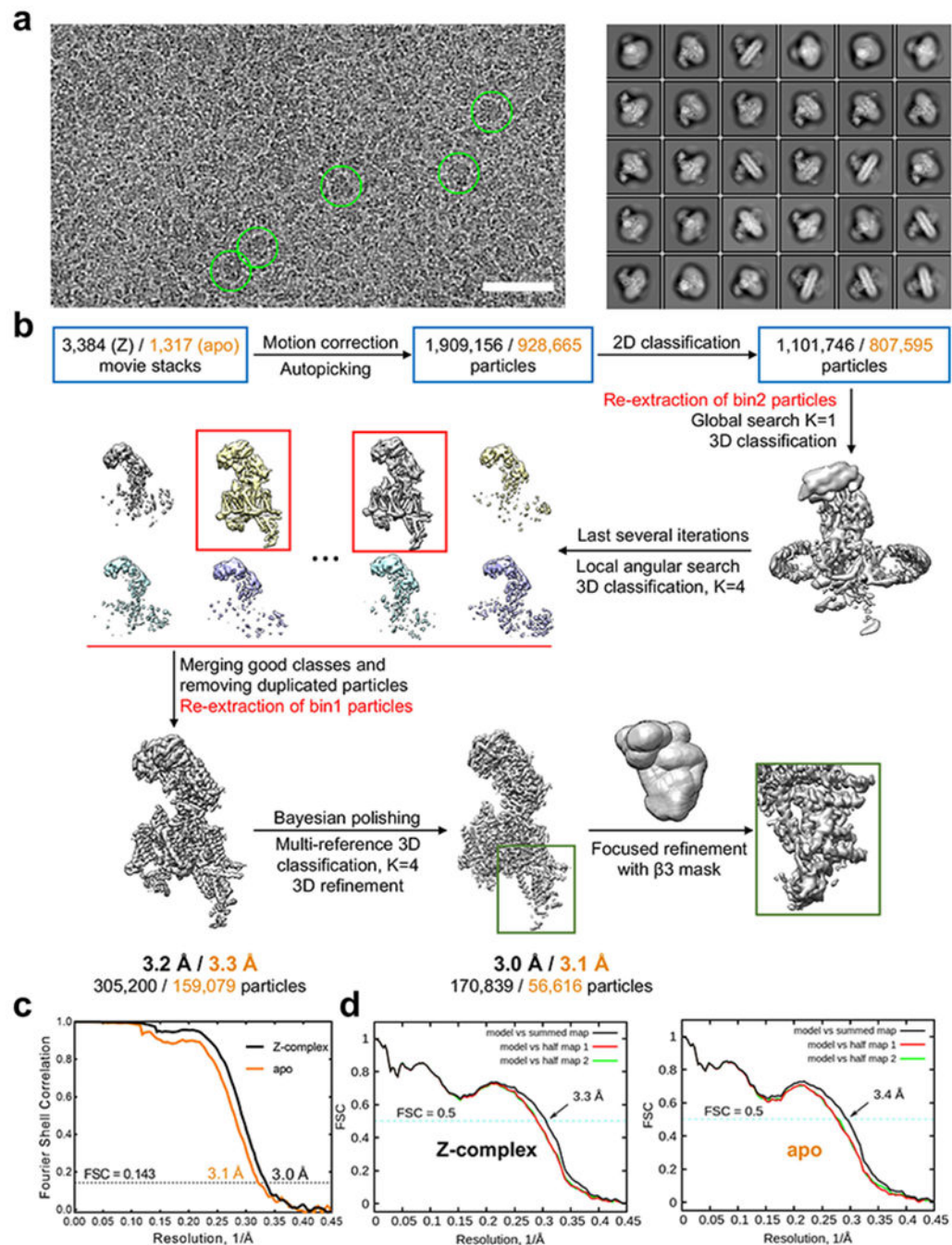
Statistics of the map reconstruction and model refinement can be found in Extended Data Table 1. All structure figures were prepared in PyMol[57].

Reporting summary

Further information on research design is available in the Nature Research Reporting Summary linked to this paper.
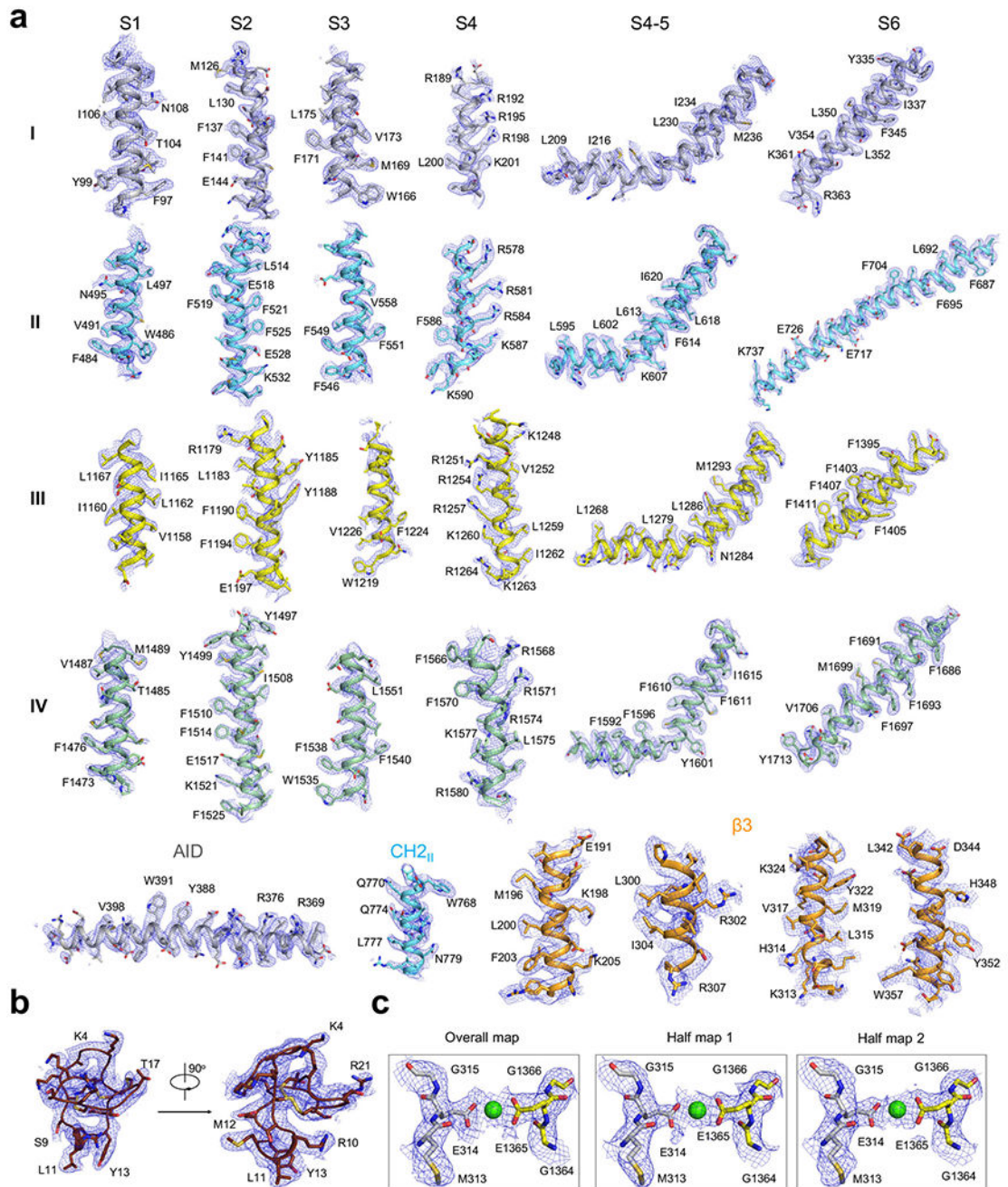
Extended Data

Extended Data Fig. 1 |. Cryo-EM analysis of the human Ca$_V$2.2 complex alone and in the presence of ziconotide.

a, Representative electron micrograph and 30 classes of 2D class averages for Ca$_V$2.2–ziconotide. The green circles indicate particles in distinct orientations. The box size for the 2D averages is 312 Å. Scale bar, 50 nm. Left, a half view of one micrograph out of 3,384 in total for Ca$_V$2.2–ziconotide. **b**, Workflow for electron microscopy data processing (Methods). **c**, The gold-standard Fourier shell correlation (FSC) curves for the

3D reconstructions. The graph was prepared in GraphPad Prism. **d**, FSC curves of the refined model versus the summed map that it was refined against (black); of the model versus the first half map (red); and of the model versus the second half map (green). Z-complex, Ca$_v$2.2–ziconotide.
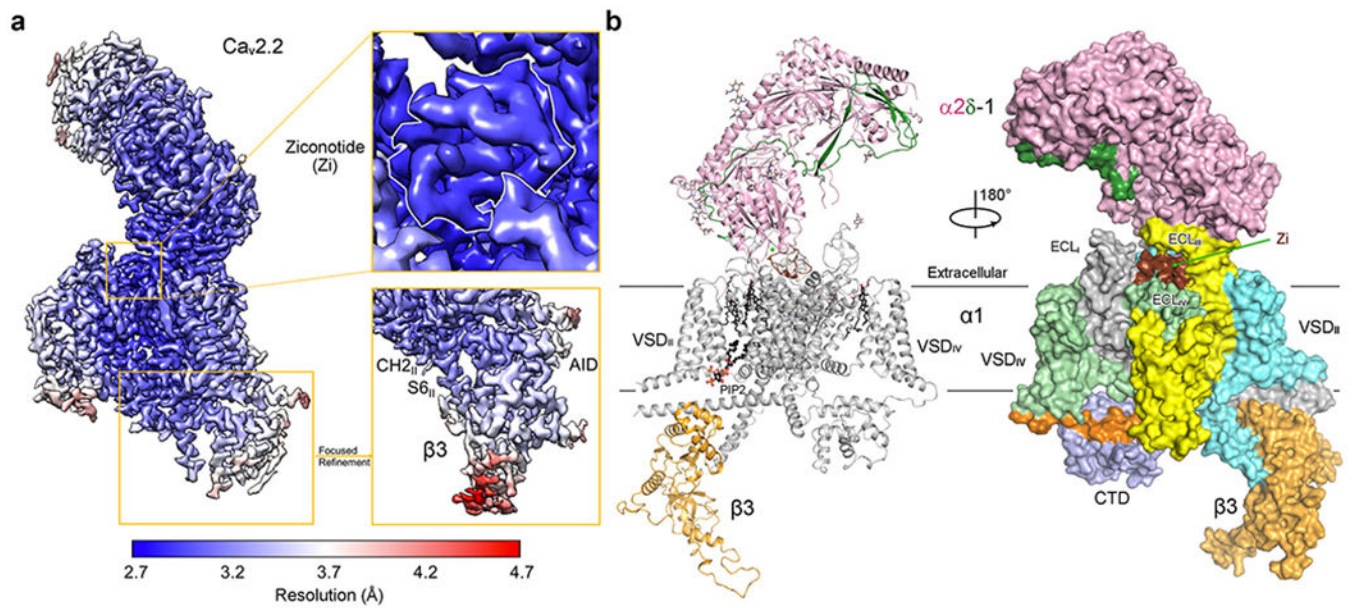

Extended Data Fig. 2 |. Cryo-EM structure of the human Ca$_v$2.2 complex bound with ziconotide.
a, Heat map for local resolution of the complex. The resolution map was calculated in Relion 3.0 and prepared in Chimera. Top inset, bound ziconotide (labelled as Zi) is well-resolved. Bottom inset, resolution of the β3 subunit, after a focused refinement, allows for reliable model building using the crystal structure of rat β3 (PDB code 1VYU) as a template. **b**, Overall structure of the complex at an averaged resolution of 3.0 Å. Left, the complex comprises the α1 core subunit (silver), the extracellular α2δ−1 subunit (light pink for α2 and green for δ) and the cytosolic β3 subunit (wheat). The peptide pore blocker ziconotide is coloured brown. The resolved lipid, cholesterol and CHS molecules are shown as black sticks. The bound PIP$_2$ is shown as black ball-and-sticks. Sugar moieties are shown as thin sticks. Right, surface presentation of the structure. The four repeats are coloured grey, cyan, yellow, and pale green. The III–IV linker and the CTD are coloured orange and pale purple, respectively.

Extended Data Fig. 3 |. Electron microscopy densities for representative segments of Ca$_V$2.2–ziconotide.

a, Electron microscopy maps for representative segments in α1 and β3. The densities for the β3 segments are from focused refinement, and the others are from the overall map. All the densities shown are contoured at 4σ. **b**, The electron microscopy map for ziconotide. **c**, Electron microscopy densities for the bound Ca^{2+} ion and surrounding residues in the selectivity filter. The maps were prepared in PyMol.
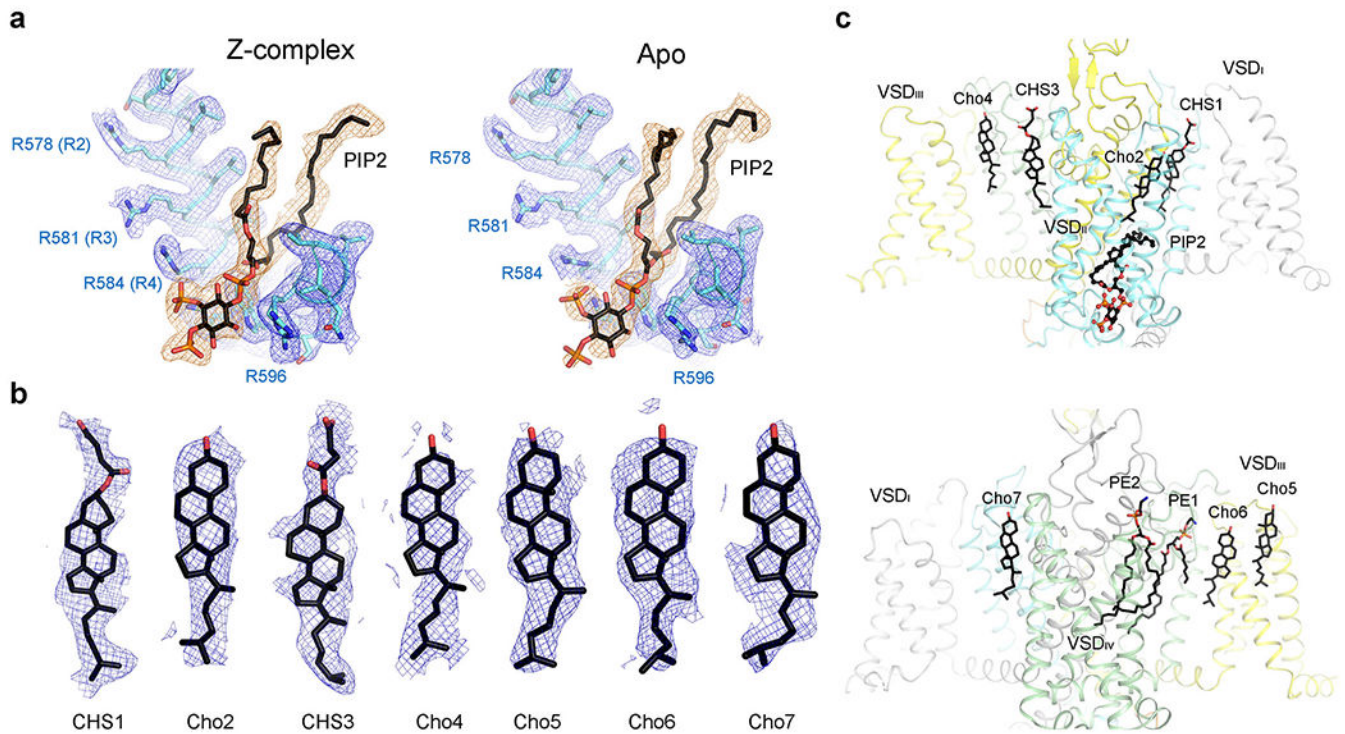
Extended Data Fig. 4 |. Lipids resolved in the structures.
a, A PIP$_2$ molecule binds to VSD$_{II}$ in both structures. All the densities shown are contoured at 3σ. **b**, The densities for the resolved cholesterol (Cho) and CHS molecules in Ca$_v$2.2–ziconotide. **c**, Lipids resolved in the structure of Ca$_v$2.2–ziconotide. The α1 subunit are shown in two opposite side views. The numbering for cholesterol and CHS is consistent with that in **b**. Two phospholipids are also resolved and assigned as phosphatidylethanolamine (PE).
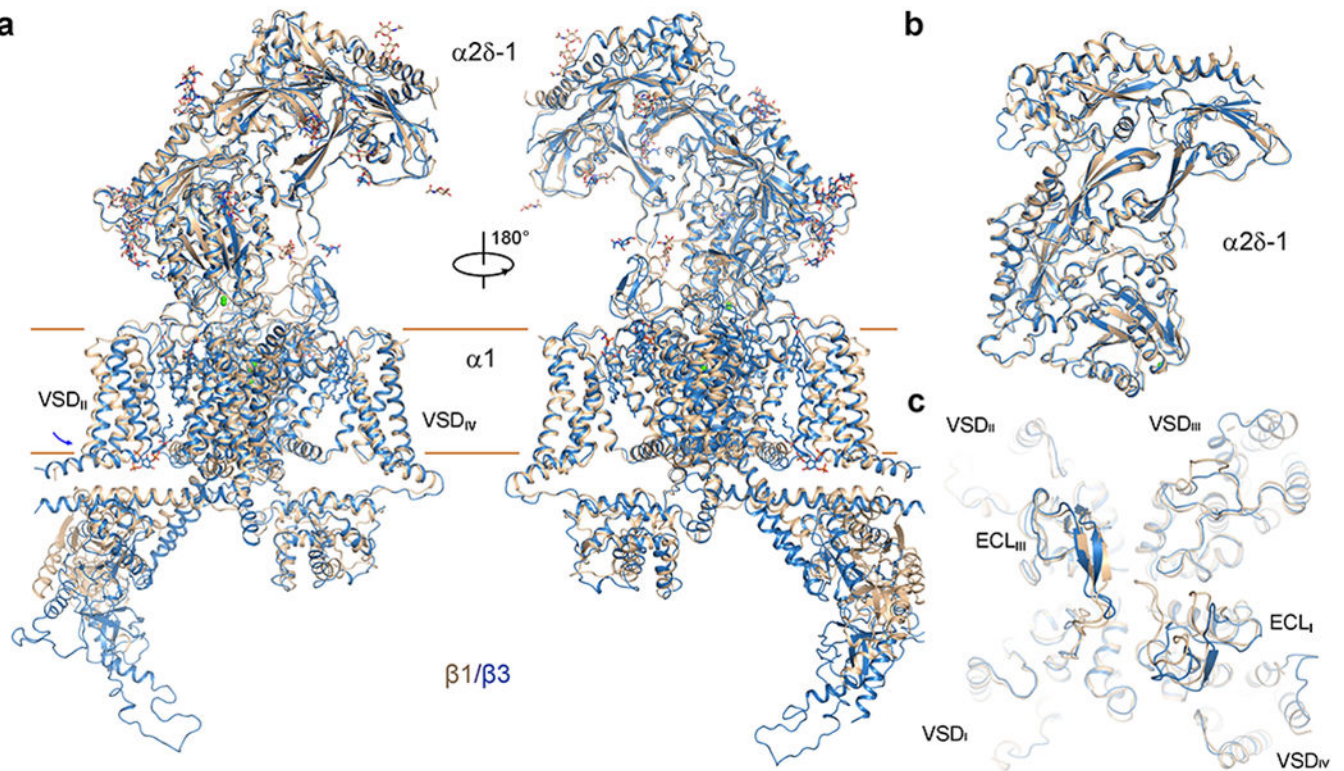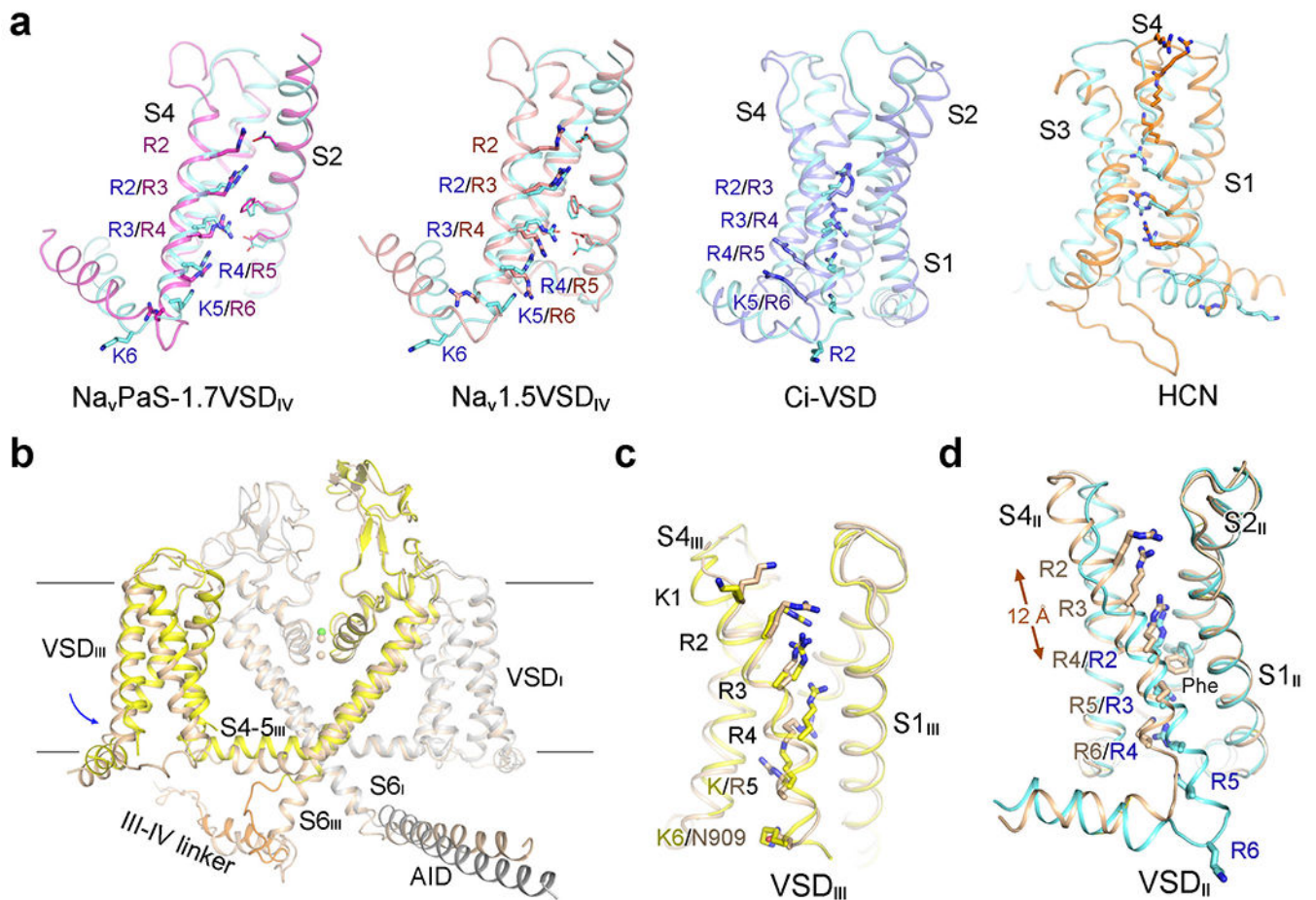
Extended Data Fig. 5 |. Structural comparison of the Ca$_v$1.1 and Ca$_v$2.2 channel complexes.
a, Superimposition of the overall structures of human Ca$_v$2.2 (apo) and rabbit Ca$_v$1.1
(PDB code 5GJW). For visual clarity, the γ subunit in the endogenous Ca$_v$1.1 complex
is not shown. The conformational shift of VSD$_{II}$ from Ca$_v$1.1 (wheat) to Ca$_v$2.2 (blue)
is indicated by the blue arrow. **b**, Identical structures of the α2δ−1 subunit in the two
channel complexes. A detailed structural description of the α2δ−1 subunit can be found in a
previous publication[18]. **c**, Structural differences of the ECLs between Ca$_v$1.1 and Ca$_v$2.2. An
extracellular view of the superimposed α1 subunits in the two channels is shown.
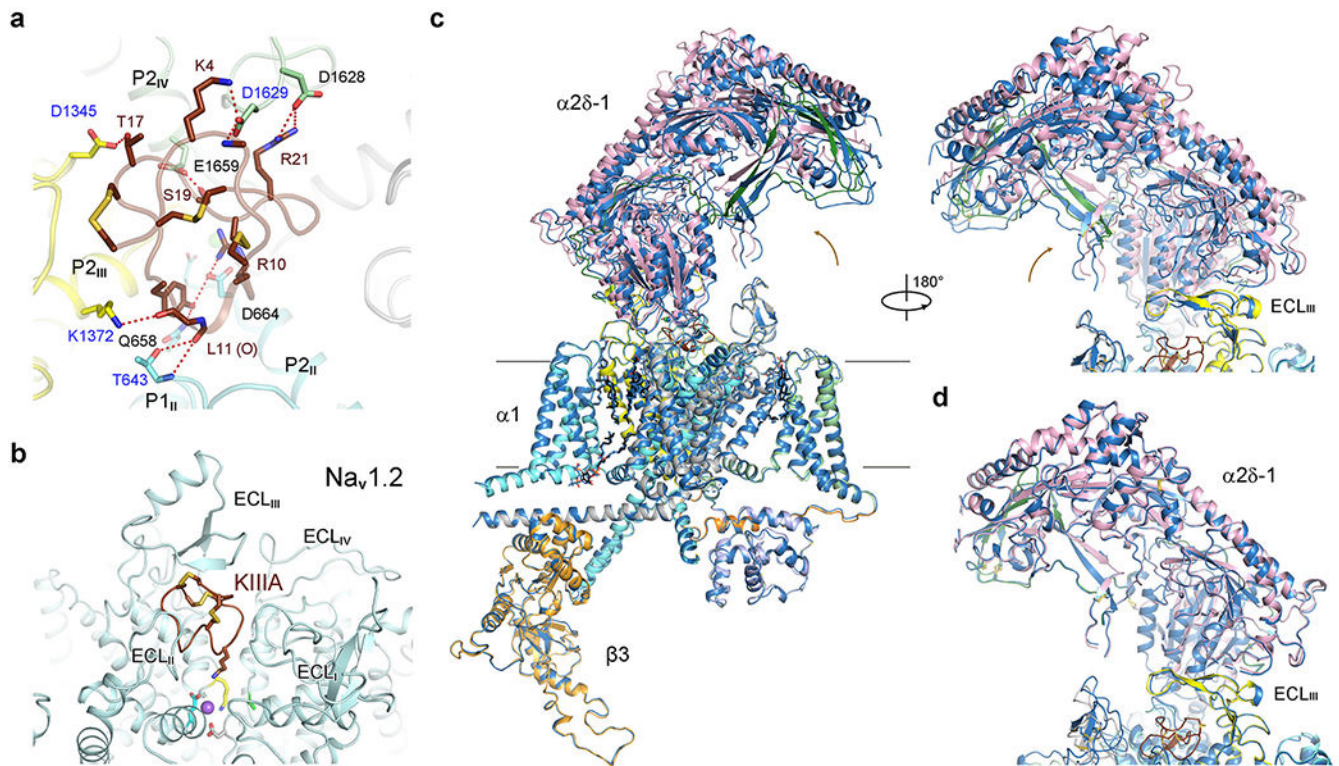
Extended Data Fig. 6 |. Conformational shifts of Ca$_v$2.2 upon ziconotide binding.
a, ECL$_I$ does not participate in ziconotide coordination. An extracellular view perpendicular to that in Fig. 1c is shown. **b**, Slightly different mode of action of KIIIA for Na$_v$1.2[26]. Lys7 in KIIIA directly blocks the outer mouth of the selectivity filter vestibule of Na$_v$1.2 (PDB code 6J8E), in a manner similar to a cork. Ziconotide lacks an equivalent basic residue. **c**, Relative shift of α2δ−1 between apo (blue) and ziconotide-bound Ca$_v$2.2 (domain-coloured) when the two structures are superimposed relative to the α1 subunit. The rest of the complex remains identical except for ECL$_{III}$. **d**, Concerted motion of α2δ−1 and ECL$_{III}$ of α1. The α2δ−1 subunit in the two structures can be superimposed with a root mean square deviation of 0.28 Å over 847 Cα atoms, indicating nearly identical conformations. When the two structures are superimposed relative to α2δ−1, the entire α1 undergoes a relative shift—except for ECL$_{III}$, which stays as a rigid body with α2δ−1.

Extended Data Fig. 7 |. Conformational changes of VSD$_{II}$ and VSD$_{III}$ between Ca$_v$1.1 and Ca$_v$2.2.

a, Structural comparison of Ca$_v$2.2 VSD$_{II}$ with other VSDs that exhibit down conformations. To make the nomenclature consistent, we define the gating charge residue on the first helical turn of the S4 segment as R1. The PDB accession codes are 6NT4 for VSD$_{IV}$ in the chimeric Na$_v$PaS-1.7, 7K18 for toxin-bound VSD$_{IV}$ in rat Na$_v$1.5, 4G80 for the antibody-locked VSD of a voltage-sensitive phosphatase, and 6UQF for the VSD of HCN1 in hyperpolarized conformation. **b**, Structural comparison of Ca$_v$1.1 and Ca$_v$2.2 shows a slight rotation of VSD$_{III}$ around the pore domain. The superimposed structures of the diagonal repeats I and III of Ca$_v$1.1 (wheat) and Ca$_v$2.2 (domain-coloured) are shown. **c**, VSD$_{III}$ remains nearly rigid in these two structures. When the structures of VSD$_{III}$ in the two channels are individually superimposed, the S4 segment and the gating charge residues align well. **d**, Marked shift of S4$_{II}$ between Ca$_v$1.1 and Ca$_v$2.2 when the two structures are compared relative to VSD$_{II}$. S4$_{II}$ undergoes a combination of spiral sliding and secondary structural transition. S1, S2 and S3 remain nearly unchanged in these two VSD$_{II}$ structures, which suggests a concerted rotation of the other three segments pivoting around S4.
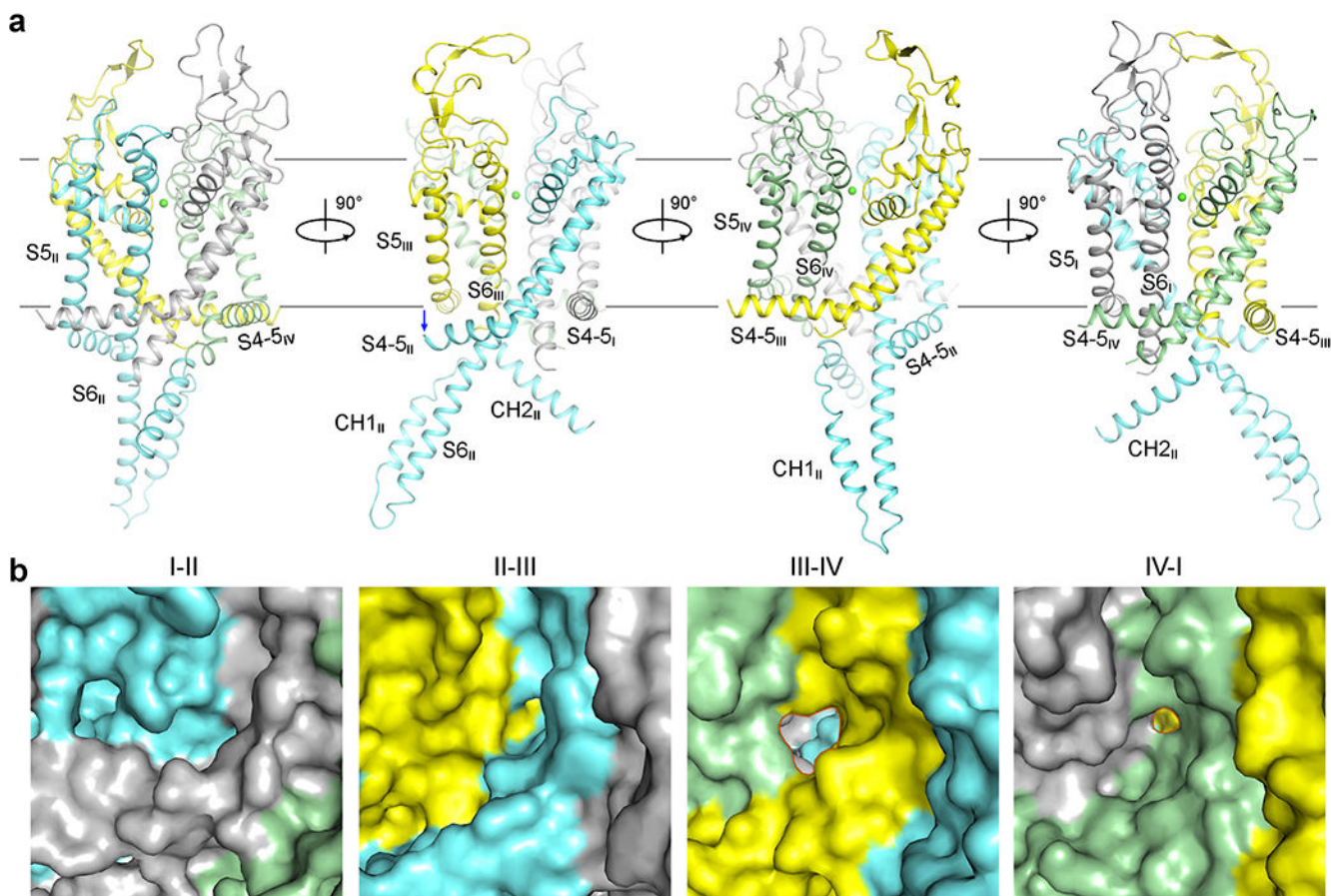
Extended Data Fig. 8 |. A closed pore domain with one small fenestration.

a, The pore domain is in a closed conformation. Four perpendicular side views of the pore domain are shown. S4–5$_{II}$ is pushed downward as a result of the sliding of S4$_{II}$. **b,** Side walls that involve S6$_{II}$ are sealed without fenestration. Side views of the pore domain surface are shown. There is only one fenestration on the interface of repeats III and IV.
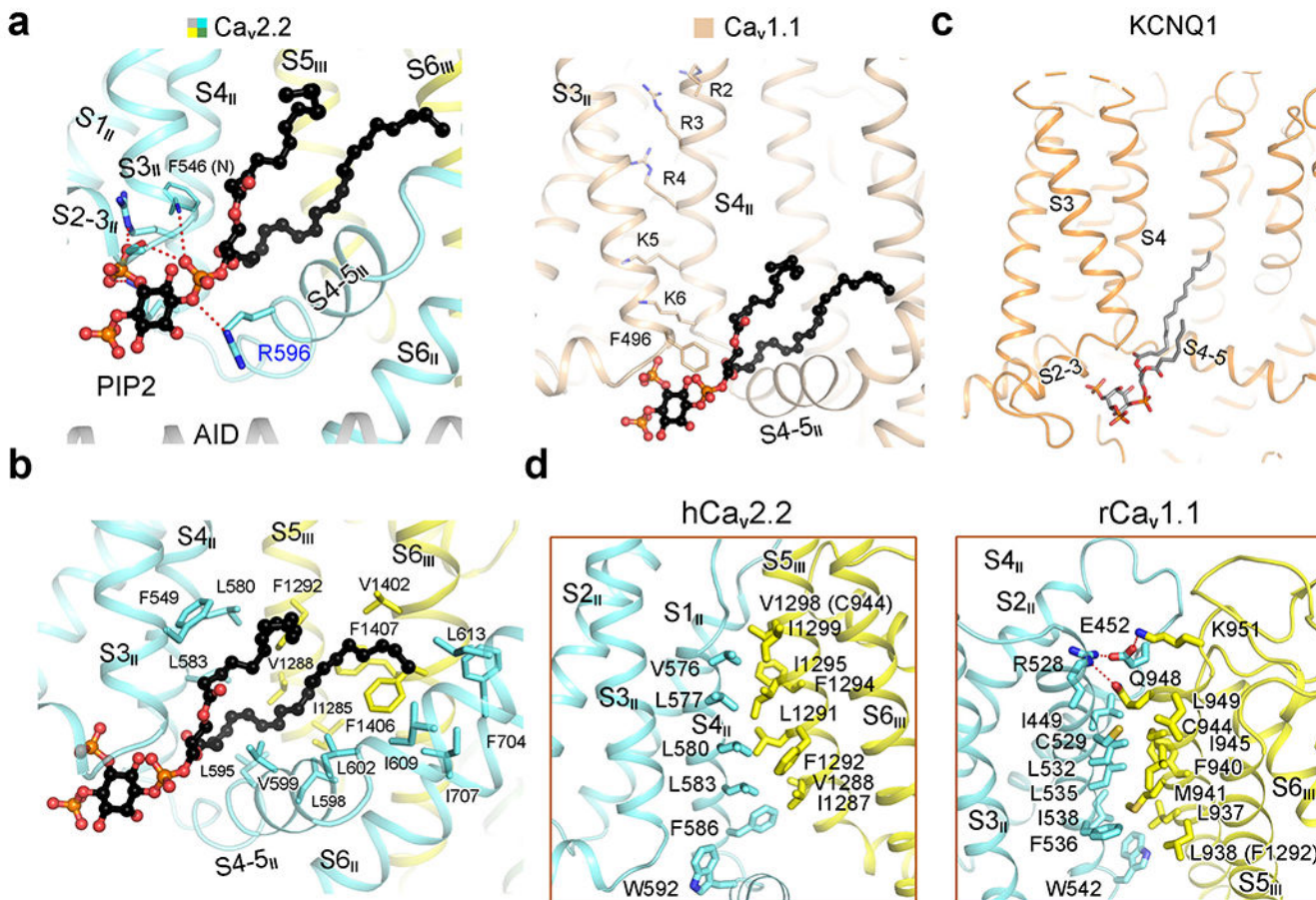
Extended Data Fig. 9 |. A PIP₂ molecule may help to stabilize the down conformation of Ca$_v$2.2 VSD$_{II}$.

a, The binding pose for PIP$_2$ is incompatible with an up VSD$_{II}$. Left, coordination of the head group of PIP$_2$ by Ca$_v$2.2. Side local view of VSD$_{II}$ is shown. Right, in an up state of VSD$_{II}$ (as in Ca$_v$1.1), R4 and K5 can no longer interact with the PIP$_2$ head group, and S4–5$_{II}$ directly clashes with PIP$_2$. Structures of Ca$_v$1.1 and Ca$_v$2.2 are superimposed relative to the α1 subunit and Ca$_v$2.2 is omitted to highlight the relative position of PIP$_2$ to Ca$_v$1.1. **b**, The hydrophobic tails of PIP$_2$ interact extensively with multiple segments in repeats II and III. Hydrophobic residues on segments S3 to S6 in repeat II and S5 and S6 in repeat III contact the two tails of PIP$_2$. **c**, The PIP$_2$ molecule in the K$_v$ channel KCNQ1 is bound at a similar, but lower, position. The PDB code for the KCNQ1 structure is 6V01. **d**, Rearrangement of the interface of VSD$_{II}$ and pore domain between Ca$_v$2.2 and Ca$_v$1.1. Ca$_v$1.1 is coloured with the same scheme as for Ca$_v$2.2. Alternative sets of hydrophobic residues between the gating charge residues on S4$_{II}$ are used for interacting with S5$_{III}$ in Ca$_v$1.1 and Ca$_v$2.2 as a result of the rotation of S4$_{II}$. The sequence numbers for corresponding VSD$_{II}$ residues in these two channels differ by 50, and those for S5$_{III}$ residues differ by 354. As labelled in the parentheses, Val1298 and Phe1292 on the S5$_{III}$ segment of Ca$_v$2.2 are at loci corresponding to Cys944 and Leu938 in Ca$_v$1.1, respectively.

Extended Data Table 1 |

Statistics for data collection and structural refinement

	Ca$_v$2.2-ziconotide (EMDB-23867) (PDB 7MIX)	Ca$_v$2.2-apo (EMDB-23868) (PDB 7MIY)
Data collection and processing		
Magnification	105,000	105,000
Voltage (kV)	300	300
Electron dose (e-/Å^2)	50	50
Defocus range (μm)	−2.1~−1.9	−2.1~−1.9
Pixel size (Å)	1.114	1.114
Symmetry	C1	C1
Initial particle images (no.)	1,909,156	928,665
Final particle images (no.)	170,839	56,616
Map resolution (Å)	3.0	3.1
FSC threshold	0.143	0.143
Map resolution range (Å)	2.8-31.2	2.9-50
Refinement		
Initial model used (PDB code)	5GJW, 1VYU, 1OMG	Ca$_v$2.2-ziconotide
Model resolution (Å)	3.3	3.4
FSC threshold	0.5	0.5
Map sharpening B factor (Å^2)	−79	−59
Model composition		
Non-hydrogen atoms	21654	21485
Protein residues	2623	2598
Ligands	28	28
B factors (Å^2)		
Protein	58.27	78.42
Ligand	69.59	62.16
R.m.s deviations		
Bond lengths (Å)	0.004	0.003
Bond angles (°)	0.759	0.727
Validation		
MolProbity score	2.00	1.95
Clashscore	9.72	9.68
Poor rotamers (%)	1.47	1.31
Ramachandran plot		
Favored (%)	94.76	94.99
Allowed (%)	5.12	4.86
Disallowed (%)	0.12	0.16

Supplementary Material

Refer to Web version on PubMed Central for supplementary material.

Acknowledgements

Data availability

The atomic coordinates and electron microscopy maps for Ca$_v$2.2 in complex with ziconotide and alone have been deposited in the PDB with the accession codes 7MIX (with ziconotide) and 7MIY (without ziconotide) and in the Electron Microscopy Data Bank with the codes EMD-23867 (with ziconotide) and EMD-23868 (without ziconotide), respectively. The atomic coordinates of the proteins for structural comparison in this study can be found in the PDB: rabbit Ca$_v$1.1 (5GJW) (https://www.rcsb.org/structure/5GJW), toxin-bound human Na$_v$1.2 (6J8E) (https://www.rcsb.org/structure/6J8E), toxin-bound Na$_v$PaS-1.7 chimera (6NT4) (https://www.rcsb.org/structure/6NT4), toxin-bound rat Na$_v$1.5 (7K18) (https://www.rcsb.org/structure/7K18), Ci-VSP (4G80) (https://www.rcsb.org/structure/4G80), HCN1 (6UQF) (https://www.rcsb.org/structure/6UQF) and KCNQ1 (6V01) (https://www.rcsb.org/structure/6V01). Expression plasmids for the Ca$_v$2.2 subunits are available from the corresponding author upon reasonable request.

References

1. Dubel SJ et al. Molecular cloning of the alpha-1 subunit of an omega-conotoxin-sensitive calcium channel. Proc. Natl Acad. Sci. USA 89, 5058–5062 (1992). [PubMed: 1317580]

2. Komuro H & Rakic P Selective role of N-type calcium channels in neuronal migration. Science 257, 806–809 (1992). [PubMed: 1323145]

3. Zamponi GW, Striessnig J, Koschak A & Dolphin AC The physiology, pathology, and pharmacology of voltage-gated calcium channels and their future therapeutic potential. Pharmacol. Rev 67, 821–870 (2015). [PubMed: 26362469]

4. Bowersox SS & Luther R Pharmacotherapeutic potential of omega-conotoxin MVIIA (SNX-111), an N-type neuronal calcium channel blocker found in the venom of Conus magus. Toxicon 36, 1651–1658 (1998). [PubMed: 9792182]

5. Miljanich GP Ziconotide: neuronal calcium channel blocker for treating severe chronic pain. Curr. Med. Chem 11, 3029–3040 (2004). [PubMed: 15578997]

6. Schmidtko A, Lötsch J, Freynhagen R & Geisslinger G Ziconotide for treatment of severe chronic pain. Lancet 375, 1569–1577 (2010). [PubMed: 20413151]

7. Lin Y, McDonough SI & Lipscombe D Alternative splicing in the voltage-sensing region of N-type CaV2.2 channels modulates channel kinetics. J. Neurophysiol 92, 2820–2830 (2004). [PubMed: 15201306]

8. Dolphin AC Voltage-gated calcium channels and their auxiliary subunits: physiology and pathophysiology and pharmacology. J. Physiol 594, 5369–5390 (2016). [PubMed: 27273705]

9. Saegusa H et al. Suppression of inflammatory and neuropathic pain symptoms in mice lacking the N-type Ca^{2+} channel. EMBO J. 20, 2349–2356 (2001). [PubMed: 11350923]

10. Snutch TP Targeting chronic and neuropathic pain: the N-type calcium channel comes of age. NeuroRx 2, 662–670 (2005). [PubMed: 16489373]

11. McGivern JG Targeting N-type and T-type calcium channels for the treatment of pain. Drug Discov. Today 11, 245–253 (2006). [PubMed: 16580601]

12. McCleskey EW et al. Omega-conotoxin: direct and persistent blockade of specific types of calcium channels in neurons but not muscle. Proc. Natl Acad. Sci. USA 84, 4327–4331 (1987). [PubMed: 2438698]

13. Ellinor PT, Zhang JF, Horne WA & Tsien RW Structural determinants of the blockade of N-type calcium channels by a peptide neurotoxin. Nature 372, 272–275 (1994). [PubMed: 7969473]

14. Stocker JW, Nadasdi L, Aldrich RW & Tsien RW Preferential interaction of ω-conotoxins with inactivated N-type Ca^{2+} channels. J. Neurosci 17, 3002–3013 (1997). [PubMed: 9096136]

15. Deer T et al. Effectiveness and safety of intrathecal ziconotide: interim analysis of the patient registry of intrathecal ziconotide management (PRIZM). Pain Pract. 18, 230–238 (2018). [PubMed: 28449352]

16. Nair AS, Poornachand A & Kodisharapu PKZiconotide: indications, adverse effects, and limitations in managing refractory chronic pain. Indian J. Palliat. Care 24, 118–119 (2018). [PubMed: 29440821]

17. Wu J et al. Structure of the voltage-gated calcium channel $Ca_v1.1$ complex. Science 350, aad2395 (2015). [PubMed: 26680202]

18. Wu J et al. Structure of the voltage-gated calcium channel $Ca_v1.1$ at 3.6 Å resolution. Nature 537, 191–196 (2016). [PubMed: 27580036]

19. Zhao Y et al. Molecular basis for ligand modulation of a mammalian voltage-gated Ca^{2+} channel. Cell 177, 1495–1506.e12 (2019). [PubMed: 31150622]

20. Zhao Y et al. Cryo-EM structures of apo and antagonist-bound human $Ca_v3.1$. Nature 576, 492–497 (2019). [PubMed: 31766050]

21. Gao S & Yan N Structural basis of the modulation of the voltage-gated calcium ion channel $Ca_v1.1$ by dihydropyridine compounds. Angew. Chem. Int. Ed. Engl 60, 3131–3137 (2021). [PubMed: 33125829]

22. Yang J, Ellinor PT, Sather WA, Zhang JF & Tsien RW Molecular determinants of Ca^{2+} selectivity and ion permeation in L-type Ca^{2+} channels. Nature 366, 158–161 (1993). [PubMed: 8232554]

23. Pragnell M et al. Calcium channel β-subunit binds to a conserved motif in the I–II cytoplasmic linker of the α1-subunit. Nature 368, 67–70 (1994). [PubMed: 7509046]

24. Kim JI, Takahashi M, Ohtake A, Wakamiya A & Sato K Tyr^{13} is essential for the activity of ω-conotoxin MVIIA and GVIA, specific N-type calcium channel blockers. Biochem. Biophys. Res. Commun 206, 449–454 (1995). [PubMed: 7826361]

25. Benjamin ER et al. Pharmacological characterization of recombinant N-type calcium channel ($Ca_v2.2$) mediated calcium mobilization using FLIPR. Biochem. Pharmacol 72, 770–782 (2006). [PubMed: 16844100]

26. Pan X et al. Molecular basis for pore blockade of human Na^+ channel $Na_v1.2$ by the μ-conotoxin KIIIA. Science 363, 1309–1313 (2019). [PubMed: 30765605]

27. Sousa SR et al. Novel analgesic ω-conotoxins from the vermivorous cone snail Conus moncuri provide new insights into the evolution of conopeptides. Sci. Rep 8, 13397 (2018). [PubMed: 30194442]

28. Nadasdi L et al. Structure-activity analysis of a Conus peptide blocker of N-type neuronal calcium channels. Biochemistry 34, 8076–8081 (1995). [PubMed: 7794920]

29. Mould J et al. The α2δ auxiliary subunit reduces affinity of ω-conotoxins for recombinant N-type ($Ca_v2.2$) calcium channels. J. Biol. Chem 279, 34705–34714 (2004). [PubMed: 15166237]

30. Chen YH et al. Structural basis of the α1–β subunit interaction of voltage-gated Ca^{2+} channels. Nature 429, 675–680 (2004). [PubMed: 15170217]

31. Van Petegem F, Clark KA, Chatelain FC & Minor DL Jr. Structure of a complex between a voltage-gated calcium channel β-subunit and an α-subunit domain. Nature 429, 671–675 (2004). [PubMed: 15141227]

32. Opatowsky Y, Chen CC, Campbell KP & Hirsch JA Structural analysis of the voltage-dependent calcium channel β subunit functional core and its complex with the α1 interaction domain. Neuron 42, 387–399 (2004). [PubMed: 15134636]

33. Clairfeuille T et al. Structural basis of α-scorpion toxin action on Nav channels. Science 363, eaav8573 (2019). [PubMed: 30733386]

34. Jiang D et al. Structural basis for voltage-sensor trapping of the cardiac sodium channel by a deathstalker scorpion toxin. Nat. Commun 12, 128 (2021). [PubMed: 33397917]

35. Sun J & MacKinnon R Structural basis of human KCNQ1 modulation and gating. Cell 180, 340–347.e9 (2020). [PubMed: 31883792]

36. Wu L, Bauer CS, Zhen XG, Xie C & Yang J Dual regulation of voltage-gated calcium channels by PtdIns(4,5)P$_2$. Nature 419, 947–952 (2002). [PubMed: 12410316]

37. Rodríguez-Menchaca AA, Adney SK, Zhou L & Logothetis DE Dual regulation of voltage-sensitive ion channels by PIP$_2$. Front. Pharmacol 3, 170 (2012). [PubMed: 23055973]

38. Mastronarde DN Automated electron microscope tomography using robust prediction of specimen movements. J. Struct. Biol 152, 36–51 (2005). [PubMed: 16182563]

39. Zheng SQ et al. MotionCor2: anisotropic correction of beam-induced motion for improved cryo-electron microscopy. Nat. Methods 14, 331–332 (2017). [PubMed: 28250466]

40. Zhang K Gctf: real-time CTF determination and correction. J. Struct. Biol 193, 1–12 (2016). [PubMed: 26592709]

41. Zivanov J et al. New tools for automated high-resolution cryo-EM structure determination in RELION-3. eLife 7, e42166 (2018). [PubMed: 30412051]

42. Rosenthal PB & Henderson R Optimal determination of particle orientation, absolute hand, and contrast loss in single-particle electron cryomicroscopy. J. Mol. Biol 333, 721–745 (2003). [PubMed: 14568533]

43. Chen S et al. High-resolution noise substitution to measure overfitting and validate resolution in 3D structure determination by single particle electron cryomicroscopy. Ultramicroscopy 135, 24–35 (2013). [PubMed: 23872039]

44. Nowycky MC, Fox AP & Tsien RW Three types of neuronal calcium channel with different calcium agonist sensitivity. Nature 316, 440–443 (1985). [PubMed: 2410796]

45. Waterhouse A et al. SWISS-MODEL: homology modelling of protein structures and complexes. Nucleic Acids Res. 46, W296–W303 (2018). [PubMed: 29788355]

46. Pettersen EF et al. UCSF Chimera—a visualization system for exploratory research and analysis. J. Comput. Chem 25, 1605–1612 (2004). [PubMed: 15264254]

47. Emsley P, Lohkamp B, Scott WG & Cowtan K Features and development of Coot. Acta Crystallogr. D 66, 486–501 (2010). [PubMed: 20383002]

48. Adams PD et al. PHENIX: a comprehensive Python-based system for macromolecular structure solution. Acta Crystallogr. D 66, 213–221 (2010). [PubMed: 20124702]

49. Shen H et al. Structure of a eukaryotic voltage-gated sodium channel at near-atomic resolution. Science 355, eaal4326](2017). [PubMed: 28183995]

50. Yan Z et al. Structure of the Na$_v$1.4-β1 complex from electric eel. Cell 170, 470–482.e11 (2017). [PubMed: 28735751]

51. Shen H, Liu D, Wu K, Lei J & Yan N Structures of human Nav1.7 channel in complex with auxiliary subunits and animal toxins. Science 363, 1303–1308 (2019). [PubMed: 30765606]

52. Pan X et al. Structure of the human voltage-gated sodium channel Na$_v$1.4 in complex with β1. Science 362, eaau2486](2018). [PubMed: 30190309]

53. Jiang D et al. Structure of the cardiac sodium channel. Cell 180, 122–134.e10 (2020). [PubMed: 31866066]

54. Li Z et al. Structural basis for pore blockade of the human cardiac sodium channel Na$_v$1.5 by the antiarrhythmic drug quinidine. Angew. Chem. Int. Edn Engl 60, 11474–11480(2021).

55. Pan X et al. Comparative structural analysis of human Na$_v$1.1 and Na$_v$1.5 reveals mutational hotspots for sodium channelopathies. Proc. Natl Acad. Sci. USA, 118, e2100066118 (2021). [PubMed: 33712547]

56. Li Z et al. Structure of human Na$_v$1.5 reveals the fast inactivation-related segments as a mutational hotspot for the long QT syndrome. Proc. Natl Acad. Sci. USA 118, e2100069118(2021). [PubMed: 33712541]

57. DeLano WL The PyMOL Molecular Graphics System, http://www.pymol.org (2002).
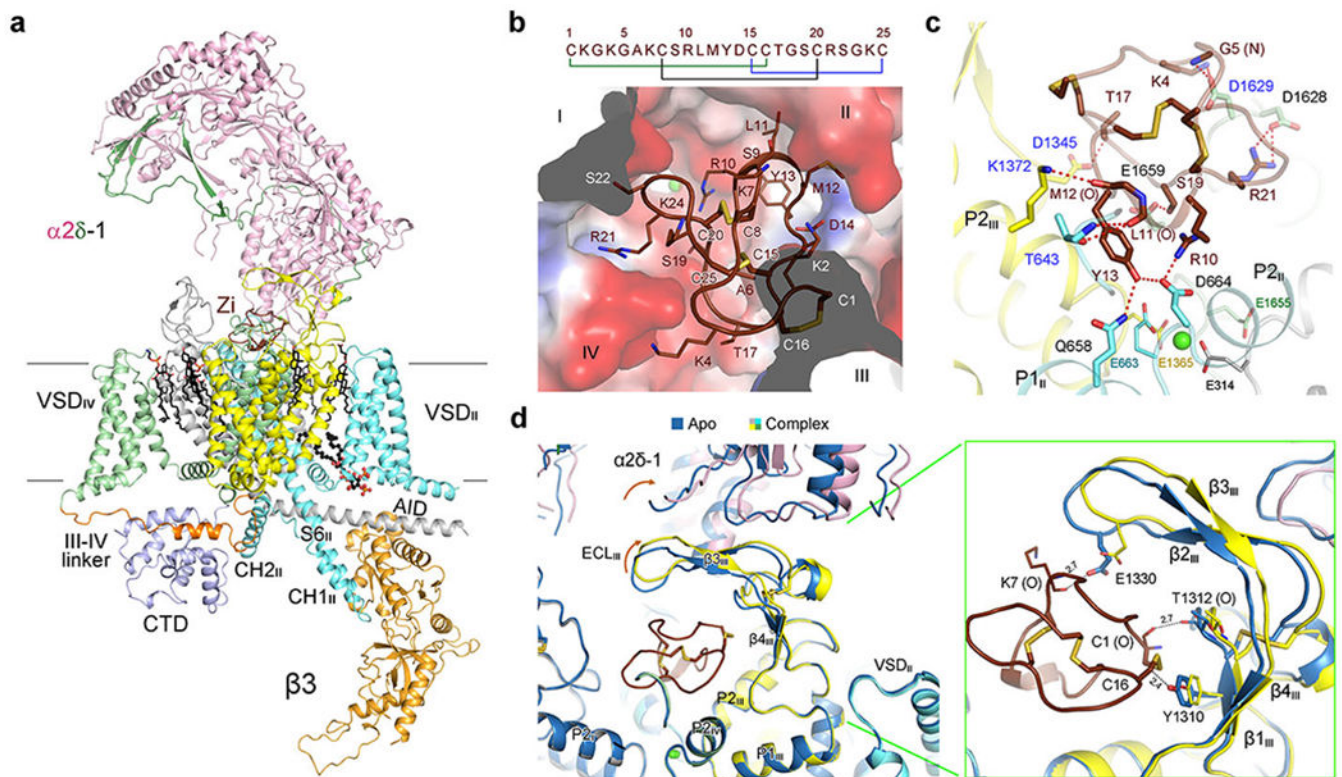
Fig. 1 |. Specific pore blockade of Ca$_v$2.2 by ziconotide.

a, Overall structure of the Ca$_v$2.2–ziconotide complex at an averaged resolution of 3.0 Å. CTD, C-terminal domain; Zi, ziconotide. The resolved lipid, cholesterol and cholesterol hemisuccinate molecules are shown as black sticks. Sugar moieties are omitted for visual clarity. All structure figures were prepared in PyMol with the same colour scheme. **b**, Ziconotide is caged by the ECLs. The sequence of ziconotide is shown above, with the three disulfide bonds indicated. The surface electrostatic potential, shown in semi-transparent presentation, was calculated in PyMol. **c**, Specific coordination of ziconotide by α1 of Ca$_v$2.2. The residues that are not conserved in Ca$_v$ channels are labelled blue (in all Figures). The bound Ca^{2+} is shown as green sphere, and the EEEE motif (Glu314, Glu663, Glu1365 and Glu1655) that determines Ca^{2+} selectivity is shown as thin sticks. Letters in parentheses denote backbone groups, N for amide and O for carbonyl oxygen (in all Figures) **d**, ECL$_{III}$ and α2δ−1 concertedly move upward to accommodate ziconotide. When the structures of the Ca$_v$2.2–ziconotide (coloured according to domain) and apo Ca$_v$2.2 (blue) are superimposed relative to α1, the only deviation (indicated by orange arrows) occurs in ECL$_{III}$ and α2δ−1. Inset, upward shift of ECL$_{III}$ to avoid clash with ziconotide. The distances between the indicated residues are in Å.
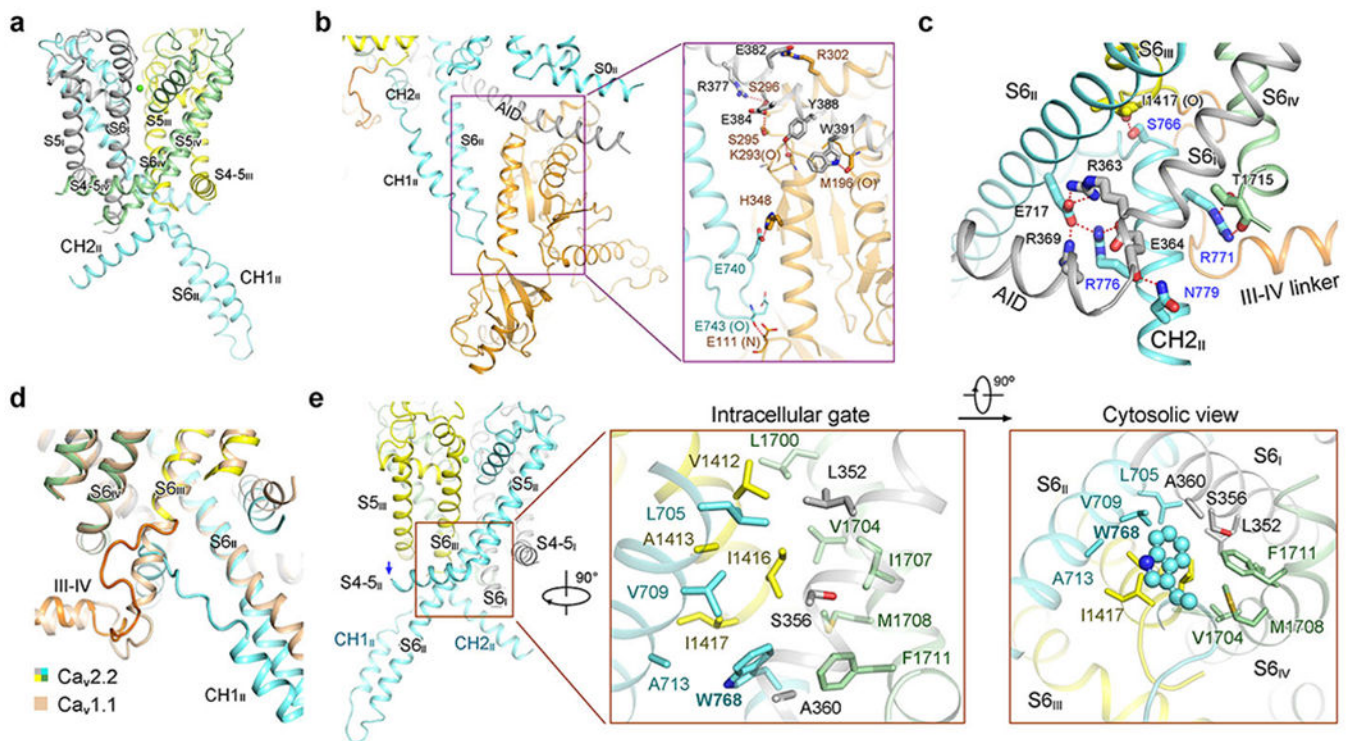
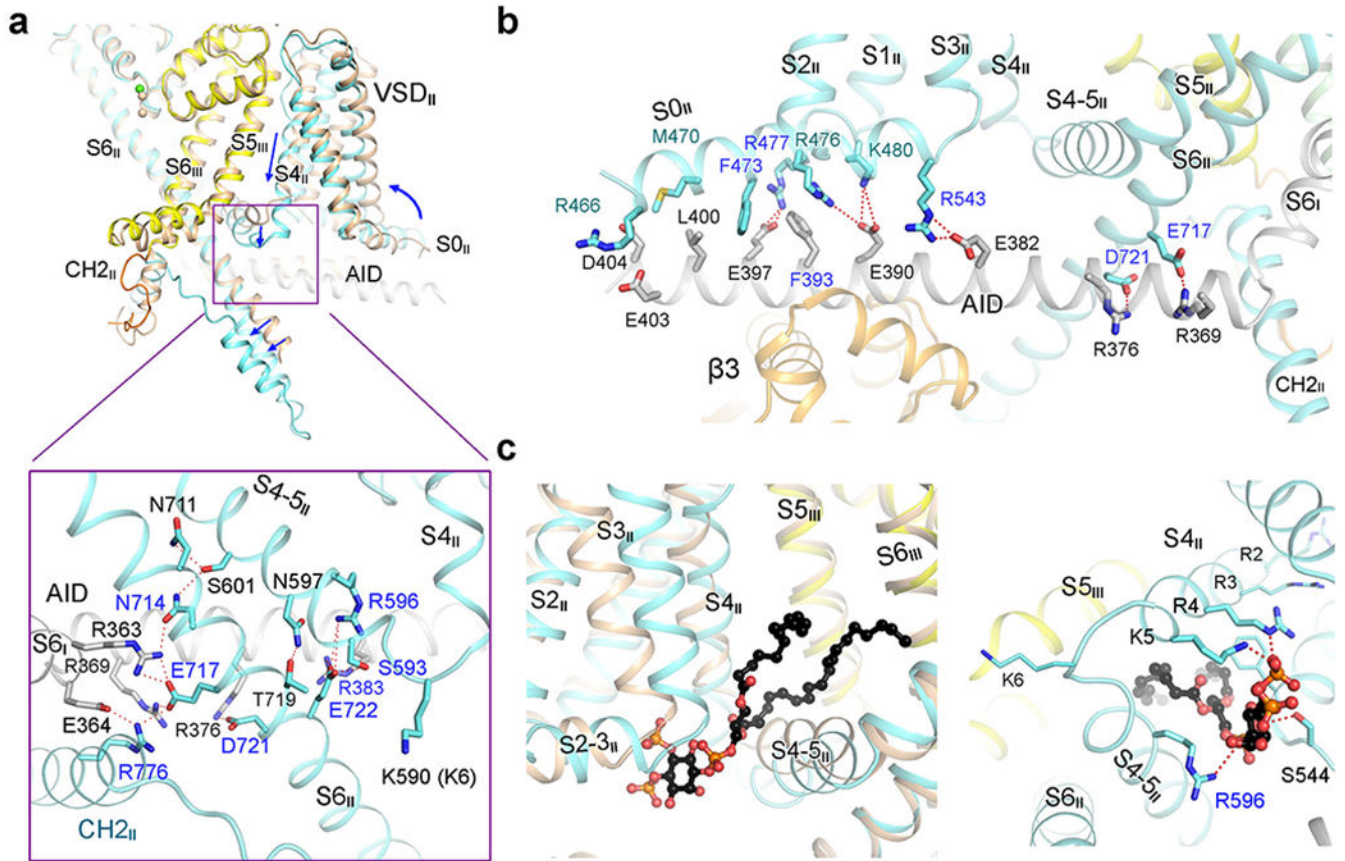**Fig. 2 |. Cytosolic segments unique to Ca$_v$2 in the II–III linker.**
a, An extended cytosolic segment of S6$_{II}$ is followed by CH1 and CH2. The sequence for S6$_{II}$C (residues 714–742) is not conserved among the Ca$_v$ family and the ensuing helices are missing in Ca$_v$1 and Ca$_v$3 channels. Supplementary Fig. 1 shows the sequence alignment. **b**, β3 is sandwiched between the AID helix and S6$_{II}$C. Inset, detailed interactions between α1 and β3. Polar interactions are indicated by red dashed lines. **c**, CH2$_{II}$ simultaneously interacts with all four S6 segments below the intracellular gate. A tilted side view of the S6 tetrahelical bundle is shown. **d**, S6$_{III}$ is three helical turns shorter in Ca$_v$2.2 than in Ca$_v$1.1. Unwinding the last three turns of S6$_{III}$ yields space to accommodate CH2$_{II}$. Ca$_v$1.1 (Protein Data Bank (PDB) code 5GJW) is coloured in wheat. **e**, CH2$_{II}$ tightens the closed intracellular gate. Several layers of hydrophobic residues on the S6 tetrahelical bundle intertwine to close the intracellular gate. Trp768, a Ca$_v$2-specific residue, interacts with several gating residues.
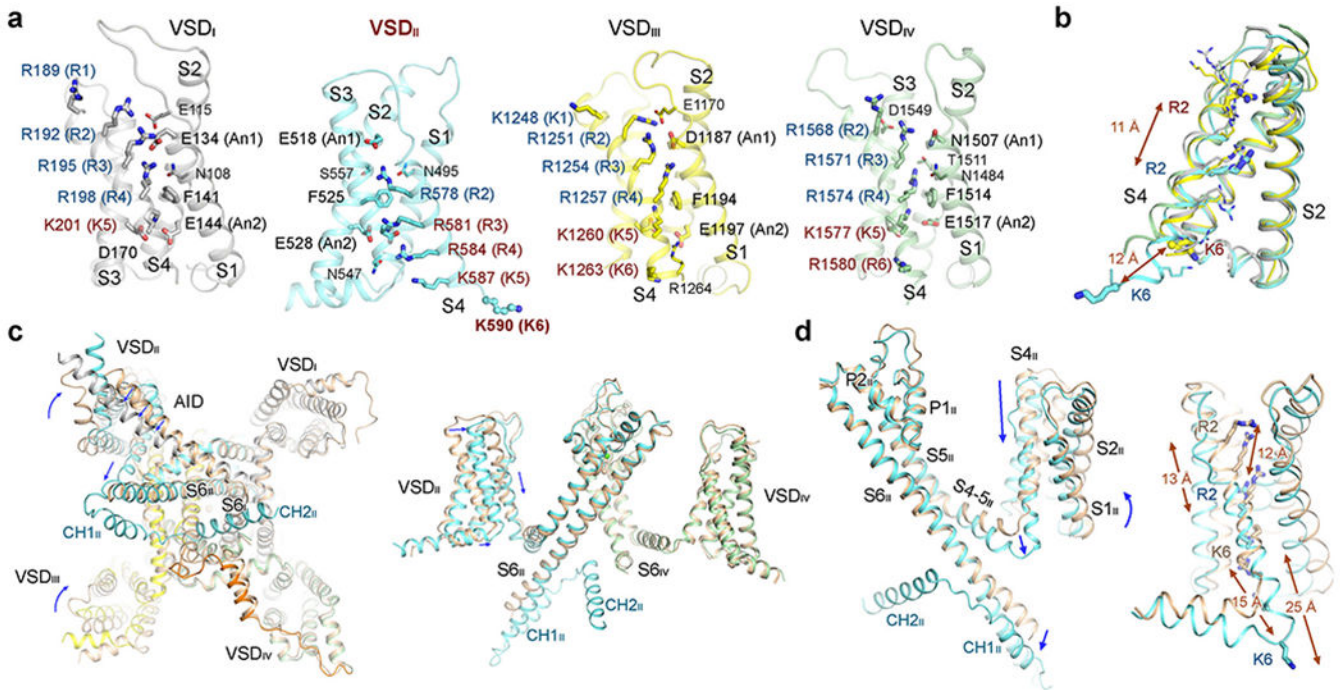
Fig. 3 |. VSD_II in a down state.
a, Structure of the four VSDs. In each VSD, the gating charge residues (gating charge numbering in parentheses) on S4 and the surrounding residues that may facilitate gating charge transfer are shown as sticks. An1, An2, conserved acidic or polar residues on S2. The gating charge residues above and below the occluding Phe on S2 are labelled dark cyan and brown, respectively. **b**, Distinct conformation of VSD_II. When the four VSDs are superimposed, $S4_{II}$ slides down by about 12 Å compared to the S4 segments in other VSDs. **c**, Conformational changes of the α1 subunit in $Ca_v1.1$ and $Ca_v2.2$. A cytosolic view of the superimposed α1 structures is shown; the CTD is omitted for clarity. The major structural shifts from $Ca_v1.1$ to $Ca_v2.2$ are indicated by blue arrows. Right, structural comparison of the diagonal repeats II and IV. **d**, Coupled shifts of VSD_II and $S6_{II}$. Left, the downward motion of $S4_{II}$ is accompanied by the rotation of VSD_II and the displacement of $S4–5_{II}$ and the nearby $S6_{II}C$. Right, pronounced shifts of VSD_II between $Ca_v1.1$ and $Ca_v2.2$ in the context of the overall α1 structure. The distances shown on the left and right indicate the linear displacement of the Cα atoms and side chains of the corresponding gating charge residues, respectively. Supplementary Video 2 shows the conformational shifts.

Fig. 4 |. The down conformation of VSD$_{II}$ is stabilized by several intracellular segments and a bound PIP$_2$.

a, Cytosolic segments that are unique to Ca$_v$2 stabilize the down VSD$_{II}$. Inset, a network of extensive polar interactions among the AID helix, S4–5$_{II}$, S6$_{II}$ and CH2$_{II}$. **b**, The AID helix is an organizing centre for segments within and near VSD$_{II}$. The straight AID helix, in addition to mediating the channel modulation by the β subunits, may serve as a lever that couples the motion of VSD$_{II}$ to S6$_I$ and S6$_{II}$. **c**, The bound PIP$_2$ favours a down conformation of VSD$_{II}$. Left, VSD$_{II}$ and the ensuing S4–5$_{II}$ in the up conformation as in Ca$_v$1.1 (wheat) would clash with PIP$_2$ in its current binding pose. Right, a cytosolic view of PIP$_2$ coordination by polar residues in Ca$_v$2.2 (coloured according to domain).